



# Defining Earth's elusive thermal budget in the presence of a hidden reservoir

Amy L. Ferrick\*, Jun Korenaga

Department of Earth and Planetary Sciences, Yale University, New Haven, CT 06511, USA



## ARTICLE INFO

### Article history:

Received 30 March 2022

Received in revised form 29 September 2022

Accepted 30 October 2022

Available online xxx

Editor: R. Dasgupta

### Keywords:

basal magma ocean

hidden geochemical reservoir

bulk silicate Earth heat production

## ABSTRACT

A hidden geochemical reservoir has long been a popular concept in the solid Earth sciences, often invoked to explain geochemical paradoxes. Easily overlooked, however, is that such a hidden reservoir invalidates traditional estimates of bulk silicate Earth (BSE) composition, including BSE heat production. Unconstrained BSE heat production threatens our ability to model Earth's thermal evolution. We present a novel method for estimating BSE heat production in the presence of a basal magma ocean—a putative hidden reservoir that has been linked to deep mantle seismic anomalies known as ultralow velocity zones. Our model tracks the thermal evolution of a fully coupled mantle, basal magma ocean, and core. Monte Carlo sampling, together with constraints on upper mantle cooling history and a physical bound on the degree of fractional crystallization, quantifies the major characteristics of Earth's thermal evolution. Chief among these constraints is the previously undefined present-day BSE heat production, which we estimate to be  $19 \pm 3$  TW. Our approach resolves the fundamental difficulty of self-consistent thermal modeling in the presence of a hidden geochemical reservoir, while simultaneously exploring the relevant parameter space. The mantle budget of non-heat-producing elements may require substantial revisions.

© 2022 Elsevier B.V. All rights reserved.

## 1. Introduction

The chemical composition of the bulk silicate Earth (BSE) sheds light on various formation processes on the early Earth as well as the composition of present-day silicate reservoirs (McDonough and Sun, 1995; Kaminski and Javoy, 2013); it also prescribes the amount of BSE heat production from the decay of U, Th, and K. BSE composition is thus essential to understanding the thermal budget of Earth, which dictates Earth's long-term thermal and chemical evolution. Yet, our current estimates of BSE composition are jeopardized by one of the most popular geochemical concepts—a hidden geochemical reservoir. The BSE composition is the average composition of all silicate reservoirs, and, compared to individual silicate reservoirs that we can directly sample (e.g., the continental crust), it must be estimated using a more theoretical approach. Traditionally, BSE composition models assume the BSE retains chondritic ratios of refractory lithophile elements (e.g., Al, Ca, Ti, rare Earth elements, Th, U). In practice, this means imposing the chondritic ratios of these elements on the compositional trends in mantle rocks (McDonough and Sun, 1995; Palme and O'Neill, 2003; Lyubetskaya and Korenaga, 2007). The chondritic constraint

must be applied to the entirety of silicate reservoirs; yet, we cannot sample the lower mantle. As a result, these traditional BSE models must further assume that the mantle is well-homogenized and that the BSE lies on the upper mantle compositional trends (McDonough and Sun, 1995; Lyubetskaya and Korenaga, 2007). A problem, then, arises in the existence of an unsampled mantle reservoir (Korenaga, 2009). Such a scenario violates the well-mixed mantle assumption of traditional BSE composition models, which consequently must be abandoned. An alarming and underappreciated result is that models of terrestrial evolution that incorporate a hidden geochemical reservoir cannot use traditional estimates of BSE heat production. Thus, we are faced with two major dilemmas in the case of a hidden geochemical reservoir. First, how can we model Earth's evolution? And second, how can we constrain BSE heat production? We offer a novel approach to modeling the thermal evolution of Earth even in the presence of a hidden silicate reservoir, and, in doing so, constrain BSE heat production itself.

Within the BSE, three major silicate reservoirs have thus far been identified: the continental crust, the depleted mantle (DMM; i.e., source of mid-ocean ridge basalts), and the enriched mantle (EM; i.e., source of ocean island basalts). In addition to these “visible” reservoirs, several lines of evidence point to a hidden, yet-to-be sampled reservoir and therefore jeopardize estimates of BSE heat production. For decades, an isolated mantle reservoir has been argued to explain geochemical paradoxes, including

\* Corresponding author.

E-mail address: amy.ferrick@yale.edu (A.L. Ferrick).

the atmospheric budget of radiogenic argon and helium (O’Nions and Oxburgh, 1983; Allègre et al., 1996; Albarède and van der Hilst, 2002), the mantle budget of silicon (Murakami et al., 2012; Mashino et al., 2020), and the terrestrial  $^{142}\text{Nd}$  anomaly (Boyet and Carlson, 2005). A natural pitfall is to determine the composition of the hidden reservoir using the deviation of known silicate reservoirs from the expected BSE composition. However, current BSE composition models assume that there is no hidden geochemical reservoir to begin with. This approach, therefore, lacks self-consistency, and we are left with a BSE and a hidden reservoir both unconstrained in composition.

Seismic observations provide a physical characterization of a potentially unsampled mantle reservoir: regions of markedly reduced seismic velocities, about 5–50 km thick, lie above the core-mantle boundary (Garnero et al., 1998; Thorne and Garnero, 2004). These so-called ultralow velocity zones (ULVZs) can either be explained by partial melting (Williams and Garnero, 1996; Lay et al., 2004) or an intrinsic density anomaly due to iron enrichment (Wicks et al., 2017; Otsuka and Karato, 2012). Although the contribution of these two explanations is under debate, in either scenario ULVZs may be remnants of a more extensive basal magma ocean (BMO) formed early in Earth’s history. In the case of partial melting, ULVZs may be the last of the BMO itself, yet to be crystallized (Labrosse et al., 2007). In the case of a positive density anomaly, ULVZs may be the last of the BMO after it has crystallized, since the BMO becomes increasingly iron-rich as it crystallizes (Ballmer et al., 2017; Pachhai et al., 2021). It should be noted that crystallization of a BMO is not the only explanation for ULVZs. Alternative theories include core-mantle interaction (Buffett et al., 2000; Mao et al., 2006) and the presence of subducted material (Dobson and Brodholt, 2005; Liu et al., 2016). However, the possibility of a BMO is supported not only by ULVZs but also by a long-lived geodynamo, which requires core cooling and therefore higher core-mantle boundary temperatures in the past (Labrosse, 2003; Tarduno et al., 2007). Further, other features of lower mantle geophysical models, such as large low shear velocity provinces (LLSVPs) and bridgmanite-enriched ancient mantle structures (BEAMS) may also be consistent with a magma ocean origin (Pachhai et al., 2021; Gülcher et al., 2021). Notably, LLSVPs and BEAMS are also candidates for unsampled reservoirs that differ from the background mantle in their composition.

The formation of a BMO in the early Earth is likely. In the original hypothesis for BMO formation, crystallization of a global magma ocean starts in the mid-mantle, which requires intersection of the liquidus and adiabat above the core-mantle boundary (Labrosse et al., 2007). The mantle liquidus must be curved in the lowermost mantle in order for this to occur (Labrosse et al., 2007; Mosenfelder et al., 2009), but if the adiabat is curved similarly to the liquidus, mid-mantle crystallization is not guaranteed. A self-consistent thermodynamic database built from high-pressure experimental data suggests that the liquidus meets the mantle adiabat at the core-mantle boundary (Fiquet et al., 2010; Miyazaki and Korenaga, 2019), seemingly undermining the original BMO hypothesis. However, recent studies on magma ocean solidification suggest that a BMO can form in a number of different scenarios, regardless of the exact shape of the liquidus and adiabat (Ballmer et al., 2017; Miyazaki and Korenaga, 2019). For example, bottom-up crystallization is still conducive to a BMO because the dense melt is susceptible to melt percolation or gravitational overturn (Miyazaki and Korenaga, 2019).

In the BMO interpretation for ULVZs, a BMO acts as a hidden geochemical reservoir yet to be sampled. The fact that BSE heat production is undefined in this scenario reveals a fundamental difficulty of modeling terrestrial evolution with a BMO (or any form of hidden geochemical reservoir). We cannot adopt the traditional estimates of BSE heat production, their assumptions having

been violated. Further, we cannot determine BMO heat production using a mass balance argument, because the sum of the silicate reservoirs—the BSE—is unconstrained. The presence of a hidden geochemical reservoir requires that we treat BSE and BMO heat production as free parameters.

In the present study, we show that, even with a hidden geochemical reservoir that leaves BSE heat production unconstrained, thermal evolution modeling may still be conducted. Our model, which fully couples the mantle, core, and a crystallizing BMO, is paired with a Monte Carlo sampling approach, in which BSE heat production is treated as a free parameter. Internal and external consistency requirements produce an ensemble of successful models. As a result, our modeling approach constrains BSE heat production itself, thus yielding critical insights into the thermal and chemical evolution of the mantle.

## 2. Methods

Thermal evolution modeling is a straightforward approach with which to investigate radiogenic heat production, and other elements of the heat budget, within the BSE and its constituent reservoirs throughout Earth history. Running many thermal evolution models, each time randomly sampling for BSE and BMO heat production, along with a set of other poorly constrained parameters, allows us to model the range of possible thermal evolution scenarios given a crystallizing BMO. Further, evaluation of several a posteriori characteristics of a given model (e.g., consistency of mantle thermal evolution with petrological observations) can refine the set of possible evolutions. Finally, this set of successful models provides constraints on the free parameters that we originally sampled for, such as BSE heat production.

In section 2.1, we outline the construction of the thermal evolution model, and the assumptions involved, including continental growth history, surface heat flux history, CMB heat flux parameterization, lower mantle viscosity, and melt layer chemical evolution. In section 2.2, we outline the Monte Carlo sampling approach and the success criteria applied to the models.

### 2.1. Thermal evolution model

Our model consists of a thermal budget for the entire Earth (i.e., mantle, BMO, and core; Fig. 1A). The thermal evolution is coupled such that the heat flux out of the top of a given layer contributes to the heat balance of the overlying layer. This global heat balance can be numerically solved back in time when coupled with an equation for the conservation of chemical species for the melt layer, which is tied to the solid-melt phase diagram (Labrosse et al., 2007).

The solid mantle thermal budget is given by:

$$-M_M C_M \frac{dT_P}{dt} = H_M - Q_M + Q_{BMO}, \quad (1)$$

where  $M_M$  and  $C_M$  are solid mantle mass and specific heat, respectively,  $T_P$  is mantle potential temperature,  $H_M$  is solid mantle heat production, and  $Q_M$  and  $Q_{BMO}$  are heat flux out of the mantle surface and BMO surface, respectively. Henceforth, the subscripts M, BMO, and C denote solid mantle, melt layer, and core parameters, respectively. Positive  $t$  denotes time before the present. Solid mantle mass  $M_M(t)$  is the difference between the total mantle mass,  $4.0 \times 10^{24}$  kg, and melt layer mass,  $M_{BMO}(t) = 4/3\pi ((h(t) + b)^3 - b^3) \rho$ , where  $h$  is melt layer thickness,  $b$  is core radius, and  $\rho$  is melt density. Radiogenic heat of a silicate reservoir (e.g., solid mantle, BMO) is the sum of the contributions from the heat-producing elements  $^{238}\text{U}$ ,  $^{235}\text{U}$ ,  $^{232}\text{Th}$ , and  $^{40}\text{K}$ :

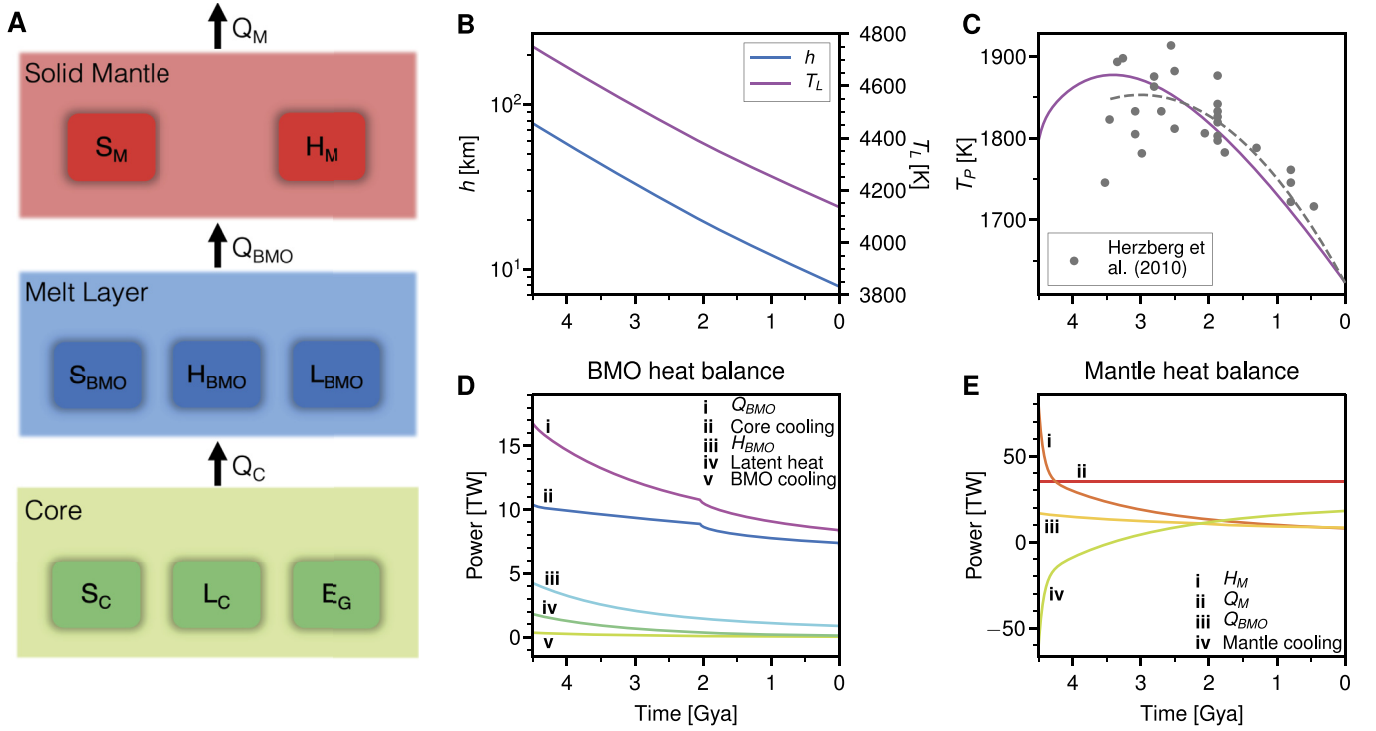


**Fig. 1.** Thermal model and evolution of a successful model. (a) Schematic of thermal model with a BMO.  $S$  refers to secular cooling,  $H$  to radiogenic heating,  $L_{BMO}$  to latent heat of BMO crystallization,  $L_C$  to latent heat of inner core solidification, and  $E_G$  to gravitational energy release from inner core formation. (b–e) Evolution of a sample successful model, including (b) melt layer thickness  $h$  and temperature  $T_L$ , (c) mantle potential temperature  $T_P$ , and heat budget for (d) the BMO and (e) the mantle. In this case, mantle heat flux is constant through Earth history. Dashed gray curve in (c) represents the reference mantle temperature used in the external consistency criterion, which is based on the petrological estimates of Herzberg et al. (2010) shown in circles. (For interpretation of the colors in the figure(s), the reader is referred to the web version of this article.)

$$H(t) = \sum_{i=1}^4 p_i m_i(0) \exp(\lambda_i t), \quad (2)$$

where  $p_i$  is an isotope's heat generation rate,  $m_i(0)$  is an isotope's present-day mass in the silicate reservoir, and  $\lambda_i$  is an isotope's decay constant. Present-day masses can be found using relative isotopic abundances and the assumed present-day heat production. To account for the growth of the continental crust on the early Earth, we implement exponential continental growth such that the mass of heat-producing elements in the crust and mantle must be adjusted over time (Rosas and Korenaga, 2018):

$$m_i^{CC}(t) = m_i^{CC}(0) e^{t\lambda_i} \left[ \frac{1 - e^{-\kappa_g(4.5\text{Gya}-t)}}{1 - e^{-\kappa_g(4.5\text{Gya})}} \right], \quad (3)$$

$$m_i^M(t) = m_i^M(0) e^{t\lambda_i} + \left[ m_i^{CC}(0) - m_i^{CC}(t) \right], \quad (4)$$

where  $\kappa_g$  is the continental growth decay constant and the superscripts CC and M refer to crustal and mantle values, respectively. When  $\kappa_g = 0.5$ , continental growth is nearly linear through Earth history; when  $\kappa_g = 17$ , continental growth occurs quickly, within the first 0.5 Ga of Earth history. Continental growth has long been controversial (see Korenaga (2021) for a review), and this range of  $\kappa_g$  (0.5 to 17) covers almost all of the so far proposed growth scenarios.

A history of mantle surface heat flux must be imposed in order to solve the global heat balance. We investigate two different end-member surface heat flux cases: (1) uniform surface heat flux through Earth history, corresponding to sluggish plate tectonics in the past (Korenaga, 2021, 2008), and (2) a nearly three-fold increase in surface heat flux in the Hadean, corresponding to a ten-fold increase in Hadean plate velocities (Miyazaki and Korenaga, 2022). Constant heat flux has the benefit of avoiding the

thermal catastrophe predicted by a conventional heat flow scaling. Although a high core heat flow may also avoid thermal catastrophe (Driscoll and Bercovici, 2014), constant surface heat flux (or equivalently, slower plate tectonics), at least back to the mid-Archean, is supported by several lines of evidence. These include the lifespan of passive margins (Bradley, 2008), the history of continental plate motion (Condie et al., 2015; Pehrsson et al., 2016), and the atmospheric budget of radiogenic xenon (Padhi et al., 2012). The second scenario tested here, wherein surface heat flux increases during the Hadean, is motivated by the possibility of rapid Hadean plate tectonics and therefore a mantle dynamics distinct from that of the Archean (Korenaga, 2021; Sleep et al., 2001). The present-day mantle heat flux in either scenario is determined by the difference between randomly sampled total surface heat flux  $Q_S(0)$  and crustal heat production  $H_{CC}(0)$ .

Melt layer heat flux,  $Q_{BMO}$ , is given by ref. (15):

$$\begin{aligned} Q_{BMO} &= 4\pi(h+b)^2 k \frac{T_L - T_M}{\delta} \\ &= -M_{BMO} C_{BMO} \frac{dT_L}{dt} + Q_C + H_{BMO} \\ &\quad - 4\pi(h+b)^2 \rho \Delta S T_L \frac{dh}{dt}, \end{aligned} \quad (5)$$

where  $k$  is solid mantle thermal conductivity,  $T_L$  is melt temperature,  $T_M$  is surface temperature of the boundary layer above the BMO,  $\delta$  is boundary layer thickness, and  $\Delta S$  is specific entropy of mantle melting. Thus, heat flux out of the top of the BMO is inversely proportional to the thickness of the thermal boundary layer above the BMO. At phase change interfaces such as that between solid and liquid, material exchange may enable highly efficient heat transfer, leading to an alternative parameterization wherein the boundary layer can become as thin as 1 km (Labrosse et al., 2018).

However, this theory cannot be directly applied for solid and melt of different composition, as is expected for the interface between the solid mantle and BMO. Here, phase transition (i.e., melting and solidification) does not take place simply by crossing the solid-melt interface, because, for most of BMO evolution, the solidus of the solid (well-mixed) mantle is unlikely to coincide with the temperature of the interface. The density difference between the solid and the (likely iron-rich) melt also prevents efficient material exchange. Under this reasoning, we parameterize boundary layer thickness using classical boundary layer arguments. Our locally-determined boundary layer thickness uses the critical Rayleigh number for boundary layer collapse (Stevenson et al., 1983) and thus is related to lower mantle viscosity:

$$\text{Ra}_c = \frac{g\alpha\rho\delta^3(T_L - T_M)}{\mu\kappa}, \quad (6)$$

where  $g$  is gravity,  $\alpha$  is coefficient of thermal expansion,  $\mu$  is boundary layer dynamic viscosity, and  $\kappa$  is thermal diffusivity. We employ the commonly-used Arrhenius form of temperature-dependent viscosity, wherein the activation energy determines the degree of temperature dependency:

$$\mu(T_L) = \mu_0 \exp\left(\frac{E + V(P - P_0)}{RT_L} - \frac{E + V(P - P_0)}{RT_M(0)}\right), \quad (7)$$

where  $\mu_0$  is a reference viscosity corresponding to the reference temperature  $T_M(0)$  and reference pressure  $P_0$ ,  $E$  is activation energy,  $V$  is activation volume,  $P$  is pressure at the interface between the solid mantle and melt layer, and  $R$  is the universal gas constant. Pressure  $P$  above the melt layer is determined using a one-dimensional Earth model (Dziewonski and Anderson, 1981). Temperature  $T_M$  at the top of the solid mantle boundary layer is related to potential temperature and depth of the boundary layer:

$$T_M(t) = T_P(t) + \frac{dT}{dz}(D - \delta(t) - h(t)), \quad (8)$$

where  $dT/dz$  is the adiabatic gradient,  $D = 2900$  km is total mantle thickness, and  $(D - \delta - h)$  is depth to the boundary layer.

Core heat flux is modeled as in Stevenson et al. (1983):

$$sQ_C = -M_C C_C \eta_C \frac{dT_L}{dt} + F_{IC}(4\pi R_i^2 \rho_C) \frac{dR_i}{dt} \frac{dT_L}{dt}, \quad (9)$$

where  $\eta_C$  relates average core temperature to  $T_L$ ,  $F_{IC}$  is an effective parameter for latent heat and gravitational energy of inner core formation, and  $R_i$  is inner core radius. Inner core radius as a function of  $T_L$  depends on known quantities and can be differentiated at every timestep to obtain  $dR_i/dT_L$  (see equations 3–5 of Stevenson et al. (1983)). The core adiabat is calculated using  $T_L$  along with the parameters used in equation 4 of Stevenson et al. (1983) (e.g.,  $T_{a1} = 3.96$  K/TPa,  $T_{a2} = -3.3$  K/TPa<sup>2</sup>). The core liquidus is calculated by choosing the zeroth-order parameter,  $T_{m0}$ , such that the liquidus and adiabat cross at the present-day inner core radius. Higher order terms are kept as those listed in Stevenson et al. (1983) (e.g.,  $T_{m1} = 6.14$  K/TPa,  $T_{m2} = -4.5$  K/TPa<sup>2</sup>).

The thermal evolution of the melt layer is tied to its chemical evolution. Because the phase diagram of the lower mantle is poorly constrained, we adopt the idealized model of Labrosse et al. (2007):

$$\frac{1}{T_A - T_B} \frac{dT_L}{dt} = \frac{3(h+b)^2 \Delta\xi}{(h+b)^3 - b^3} \frac{dh}{dt}, \quad (10)$$

where  $T_A$ ,  $T_B$ , and  $\Delta\xi$  are phase diagram parameters:  $T_A$  is melting temperature of a light component,  $T_B$  is melting temperature of a dense component, and  $\Delta\xi$  is the difference in mass fraction

**Table 1**

Parameter values used across all thermal evolution models.

Parameter	Unit	Value
$C_M$	J/kg/K	1240
$C_{BMO}$	J/kg/K	1000
$M_C$	kg	$2 \times 10^{24}$
$\eta_C$		1.2
$\rho$	kg/m <sup>3</sup>	5500
$\rho_C$	kg/m <sup>3</sup>	$1.3 \times 10^4$
$b$	km	3480
$R_i(0)$	km	1234
$k$	W/m/K	8
$\kappa$	m <sup>2</sup> /s	$10^{-6}$
$g$	m/s <sup>2</sup>	9.8
$\alpha$	K <sup>-1</sup>	$2 \times 10^{-5}$
$\Delta S$	J/kg/K	300
$T_P(0)$	K	1400
$\text{Ra}_c$		$2 \times 10^3$
$P_0$	GPa	75

**Table 2**

Parameter ranges used for Monte Carlo random sampling.

Parameter	Unit	Range
$H_{CC}(0)$	TW	[5, 10]
$H_M(0)$	TW	[3, 15]
$H_{BMO}(0)$	TW	[0.5, 8]
$Q_S(0)$	TW	[43, 49]
$h(0)$	km	[5, 10]
$T_L(0)$	K	[3100, 4200]
$T_A$	K	[5000, 6000]
$T_B$	K	[3000, 4000]
$\Delta\xi$		[0.02, 0.3]
$\log_{10} \mu_0$	Pa s	[21, 23]
$E$	kJ/mol	[30, 640]
$V$	m <sup>3</sup> /mol	[0, $10^{-5}$ ]
$dT/dz$	K/100 km	[0.03, 0.04]
$\kappa_g$	1/Gyr	[0.5, 17]
$C_C$	J/kg/K	[550, 900]
$F_{IC}$	$10^6$ J/kg	[0.5, 2]

of the dense component between the melt and the solid. Although possible chemical interactions with the core may influence the crystallization of the melt layer (see Labrosse et al., 2007), the processes controlling such interactions are poorly constrained. We therefore assume no chemical interaction occurs between the core and the melt layer.

Parameters that remain constant across all models are listed in Table 1.

## 2.2. Monte Carlo sampling

Most parameters in our model, especially those related to lower mantle and core properties, are not well-constrained experimentally or observationally. Therefore, investigating a reasonable parameter space is important for both representing all possible scenarios and determining which parameters influence model results. Additionally, developing criteria that successful models must satisfy allows us to establish a successful parameter space (i.e., one that produces both internally and externally consistent results). Thus, we use a Monte Carlo approach involving random sampling of poorly-constrained parameters. Independent parameters and their sampling ranges are listed in Table 2. Parameters are sampled from a uniform distribution. For each combination of randomly sampled parameters, equations for heat balance and mass conservation are simultaneously solved back to  $t = 4.5$  Gya.

We apply two criteria to identify successful models. First, successful models must be externally consistent; that is, they must closely reproduce a petrological estimate (Herzberg et al., 2010)

for the evolution of upper mantle temperature back to 3.5 Gya. The deviation of a model from petrological constraints on mantle temperature is determined by the following goodness of fit equation:

$$\chi^2 = \frac{\int_0^{t_{\max}} \left[ \frac{T_P(t) - T_P^{\text{ref}}(t)}{\sigma} \right]^2 dt}{t_{\max}}, \quad (11)$$

where  $\sigma = 50$  K,  $t_{\max} = 3.5$  Gya, and  $T_P^{\text{ref}}(t) = 1853 - 25.6(t - 3)^2$  is the reference mantle temperature in Kelvin corresponding to the petrological observations of Herzberg et al. (2010). Model runs with  $\chi^2 < 1$  are considered externally consistent.

The second success criterion is a physical bound on the degree of fractional crystallization in the initial global magma ocean, which is directly related to the enrichment of the BMO in heat-producing elements. This constraint is implemented as follows. For a given model, we can compare the initial concentration of heat-producing elements in the melt layer to that in the BSE:

$$\frac{H_{BMO}(4.5 \text{ Gya})}{M_{BMO}(4.5 \text{ Gya})} = f \frac{H_{BSE}(4.5 \text{ Gya})}{M_M}, \quad (12)$$

where  $H_{BMO}$  is BMO radiogenic heat production,  $H_{BSE}$  is BSE radiogenic heat production (the sum of that in the BMO, solid mantle, and continental crust),  $M_{BMO}$  is BMO mass,  $M_M$  is total mantle mass, and  $f$  is the enrichment factor of the BMO with respect to the BSE. Here,  $f$  is the output parameter and is calculated from the remaining parameters evaluated at 4.5 Gya. Different values of  $f$  correspond to different BMO formation scenarios. In the classical BMO formation scenario, a global magma ocean crystallizes both upwards and downwards, starting from some mid-mantle depth (Labrosse et al., 2007). In this case, the basal melt shares the same composition with the global melt from which it formed; the BMO will have no enrichment with respect to the BSE, and  $f = 1$ . In another possible scenario, the parent magma ocean quickly solidifies until it reaches the critical melt fraction for rheological transition, after which a BMO may form by melt percolation or Rayleigh-Taylor instability (Miyazaki and Korenaga, 2019). This critical melt fraction is commonly assumed to be 40% of the total mantle mass (Solomatov, 2015). Because heat-producing elements are highly incompatible, the entire budget of these elements will reside in the molten portion of the mantle and thus in the BMO. Since all of the heat-producing elements are in the BMO (initially 40% of the BSE), the BMO is characterized by an enrichment factor of  $f = 2.5$ . In accordance with these formation scenarios, successful models must yield a value of  $f$  within the range [1.00, 1.11] or [2.50, 3.33], where the deviations from 1 and 2.5 account for model uncertainties. Values of  $f$  below 1 cannot occur because the heat-producing elements are highly incompatible, such that the melt will not be depleted in those elements. Values of  $f$  above 3.33 are unlikely because the rheological transition is unlikely to occur below a melt fraction of 30%. For simplicity, we consider only the end-member formation scenarios discussed above, leading to the two successful  $f$  ranges. However, it should be noted that more complicated formation scenarios have been proposed, such as a combination of top-down crystallization followed by Rayleigh-Taylor overturn (Labrosse et al., 2015). In these cases, intermediate values of  $f$  may become more appropriate.

### 3. Results

We ran a total of  $2 \times 10^7$  models for each of the two surface heat flux cases that correspond to either fast or slow Hadean plate tectonics. Successful runs are rare. After requiring consistency with upper mantle thermal history, 10% of models are successful, and

after further imposing the concentration-based requirement, the success rate drops to 0.04% and 0.13% for  $1.00 < f < 1.11$  and  $2.50 < f < 3.33$ , respectively. Fortunately, our results are virtually insensitive to whether Hadean plate tectonics was fast or slow (compare Fig. 2 and Fig. S2, all panels). Henceforth, we report results for the case with constant mantle heat flux through Earth history, unless otherwise noted.

In a representative successful thermal evolution model, melt layer temperature and thickness decrease linearly and exponentially, respectively (Fig. 1B; cf. Labrosse et al., 2007). Mantle temperature increases between 4.5 Gya and 3 Gya, and then decreases until the present day (Fig. 1C). Heat from the core is the largest contributor to the melt layer heat balance (Fig. 1D), although this is not always the case and depends on several of the randomly sampled parameters, including radiogenic heat production in the melt layer. The solid mantle heat balance is initially dominated by radiogenic heating, until it is surpassed by secular cooling after 2.5 Gya (Fig. 1E). Heating from below (i.e., from the melt layer) is relatively minor; it does not surpass 15 TW throughout the evolution. In a representative successful model where surface heat flux is high in the Hadean (Fig. S1), mantle temperature initially decreases (Fig. S1A). This follows from the imposed high surface heat flux on the early Earth, which requires high (and positive) mantle secular cooling (Fig. S1D). This effect on mantle temperature is the only first-order difference between models with constant surface heat flux and those with increased Hadean surface heat flux.

The distribution of parameter evolutions for successful models (Fig. 2, S2, and S3) indicate a broad range of possible thermal evolution scenarios. Melt layer thickness varies considerably across models (Fig. 2A, B) and can be between 100 and 1000 km at 4.5 Gya. Melt layer temperature, too, is model-dependent, with nearly 2000 K variation across models at 4.5 Gya. Core heat flux typically remains constant at  $\sim 10$  TW but may decrease by a factor of 4 over Earth history (Fig. 2G, H). The inner core generally forms at around 2 Gya, but can be as old as 4.5 Gya (Fig. 2K, L). Melt layer heat flux is generally higher for the case of  $2.50 < f < 3.33$  (Fig. 2D) than the case of  $1.0 < f < 1.11$  (Fig. 2C); this is because a higher  $f$  requires the melt layer to be more enriched in heat-producing elements (equation (12)). Again, the distribution of parameter evolutions is largely insensitive to which surface heat flux case is used (Fig. 2 and S2), apart from mantle temperature (Fig. 2I, J and Fig. S2I, J).

Requiring a realistic thermal evolution yields important constraints on the acceptable range of model parameters. Prior to imposing the concentration-based requirement,  $f$  has a broad distribution and can be much larger than is reasonable (Fig. 3A).  $H_{BSE}$  positively correlates with  $f$ , a counterintuitive relationship considering the definition of  $f$  (equation (12)). We might expect that, as  $f$  increases (and the BMO is more and more enriched with respect to the BSE),  $H_{BSE}$  will decrease so that the relative enrichment of the BMO increases. However, a large  $f$  must be paired with a large  $H_{BSE}$ ; otherwise, if  $H_{BSE}$  and thus  $H_M$  are low, mantle secular cooling must be high in order to satisfy the imposed mantle heat flux. As a result, mantle temperature rises too steeply and the mantle temperature criterion is not met. The importance of the positive correlation between  $f$  and  $H_{BSE}$  is that when we impose the bounds on  $f$  (indicated by the red box in Fig. 3A), many cases with high  $H_{BSE}$  are excluded. Another interesting consequence of this constraint is that it automatically prefers models with reasonable core thermal histories (i.e., positive core heat flux through Earth history; Fig. 3A, dashed white line).

Fig. 3 presents the a posteriori distributions of selected parameters (see Fig. S4 for additional parameters, and Table 3 for parameter means and standard deviations). The BMO and BSE typically contain 2.5 TW and 18 TW of radiogenic heat production, respectively (Fig. 3B, C). Both the initial melt layer thickness

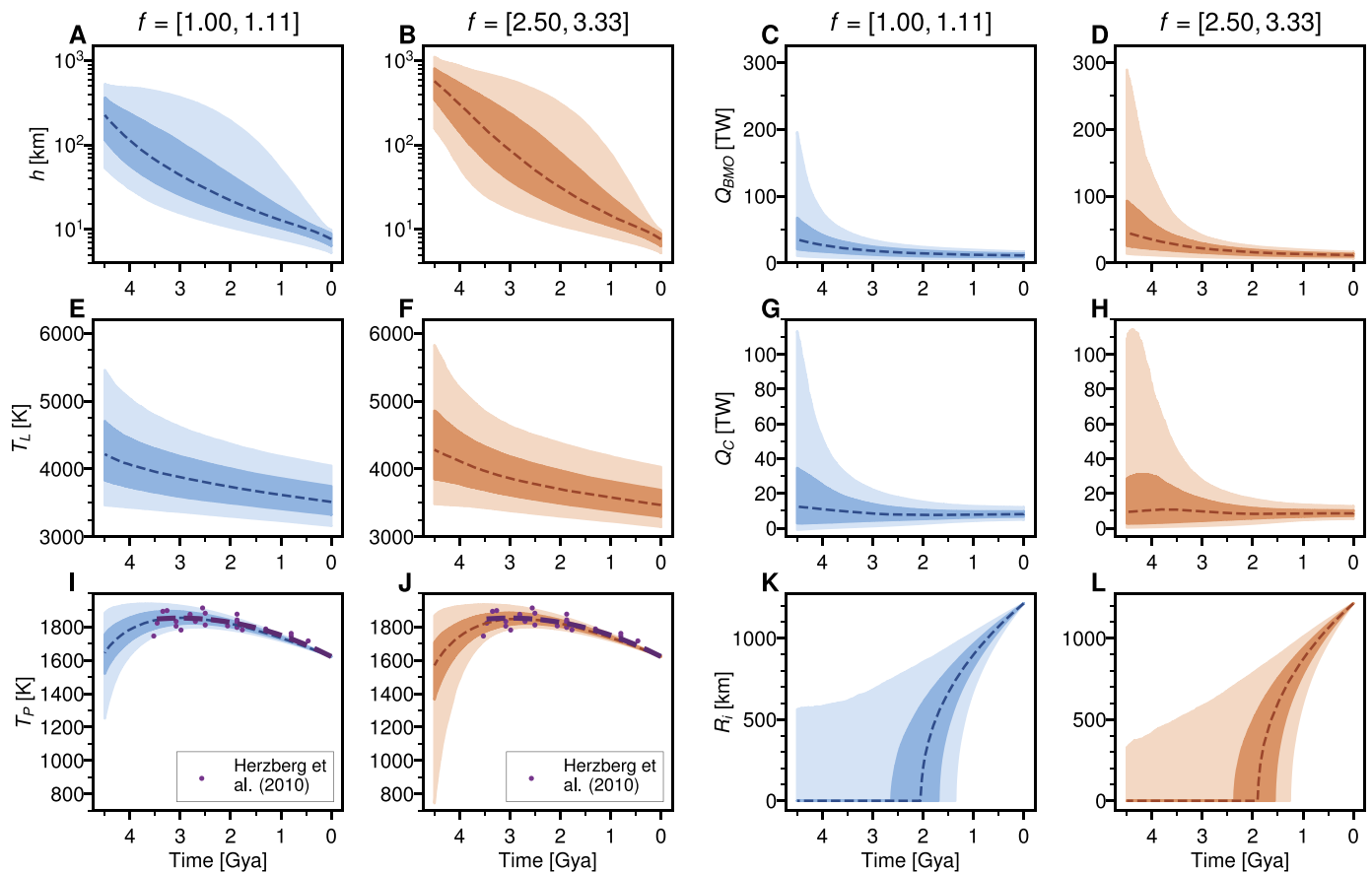


**Fig. 2.** Successful model evolutions. Distributions of successful model evolutions are shown for the case of constant mantle heat flux through Earth history. Dashed lines correspond to the median, dark shading corresponds to the middle 50%, and light shading corresponds to the middle 90%. Blue and orange shadings correspond to different ranges of the parameter  $f$  as shown at the top. (a, b) Melt layer thickness, (c, d) heat flux out of the BMO, (e, f) melt layer temperature, (g, h) heat flux out of the core, (i, j) mantle potential temperature, and (k, l) inner core radius. Dashed purple curves in (i, j) represent the reference mantle temperature used in the first criterion for successful runs, which is based on the petrological estimates of Herzberg et al. (2010) shown in circles.

(Fig. 3D) and mantle heat production (Fig. 3E) depend on  $f$  (and thus BMO formation scenario). The optimal reference viscosity is high ( $\sim 10^{23}$  Pa s; Fig. 3F), although this viscosity pertains to an intermediate reference pressure of 75 GPa. Actual viscosities of the solid mantle boundary layer ( $\sim 10^{20}$ – $10^{21}$  Pa s; Fig. S3G, H) are consistent with experimental and observational estimates for the lowermost mantle (Karato, 2008; Forte et al., 2015). On the other hand, activation energy ( $\sim 100$ – $300$  kJ/mol; Fig. 3G) is lower than experimental and theoretical estimates (Dobson et al., 2008; Karki and Khanduja, 2007). Low activation energy may be explained by grain-size-sensitive creep, wherein higher temperatures promote grain growth and thus a more sluggish rheology (Solomatov, 1996; Korenaga, 2005).

Fig. 4 presents correlations between selected parameters among successful models (see Tables S2 and S3 for correlation coefficients between all parameters). Present-day melt temperature negatively correlates with mantle heat production (Fig. 4B) and thus BSE heat production (Fig. 4C). This is because the present-day melt temperature sets the present-day heat flux from the melt layer to the solid mantle,  $Q_{BMO}$ . The components of the solid mantle heat balance must sum to the imposed surface heat flux, so if  $Q_{BMO}$  and  $H_M$  are both high or both low, secular cooling may be unreasonably low or high, respectively, and the mantle temperature criterion is not met. The strongest correlation among parameters is that between initial BMO thickness and present-day  $H_{BMO}$  (Fig. 4E). These two parameters have a correlation coefficient of 0.96, the highest among any two parameters for cases where  $1.0 < f < 1.11$  (Table S2) and for cases where  $2.5 < f < 3.33$  (Table S3). In combina-

tion, initial BMO thickness and  $H_{BMO}$  determine the concentration of heat-producing elements in the BMO, and therefore influence the value of  $f$  (see equation (12)). The criterion imposed on  $f$  means that only cases in which this concentration is reasonable are considered successful. For example, a large BMO must have a correspondingly large budget of heat-producing elements. Thus, the parameters have a strong positive correlation.

#### 4. Discussion and conclusions

Our modeling approach builds off of previous BMO evolution modeling (Labrosse et al., 2007) and includes the use of random sampling to explore the range of possible thermal evolution scenarios. Therefore, the BMO evolution presented by Labrosse et al. (2007) is captured within our range of successful models (e.g., see BMO thickness (Fig. 2A, B) and temperature (Fig. 2E, F)), along with a diversity of additional scenarios. For example, the initial size of the BMO varies substantially (Fig. 3D), as does the age of the inner core (Fig. 2K, L). Appreciating the range of possible scenarios afforded by our current knowledge is important when evaluating the implications of a BMO, such as the cooling history of the core.

A putative BMO, suggested by deep mantle seismic observations, entails a significant, often underappreciated consequence for BSE composition. The well-mixed mantle assumption having been violated, traditional cosmochemical and geochemical estimates of present-day BSE heat production,  $16 \pm 3$  TW (Lyubetskaya and Korenaga, 2007), become invalid; note that the widely-cited compositional model of McDonough and Sun (1995) provides an estimate

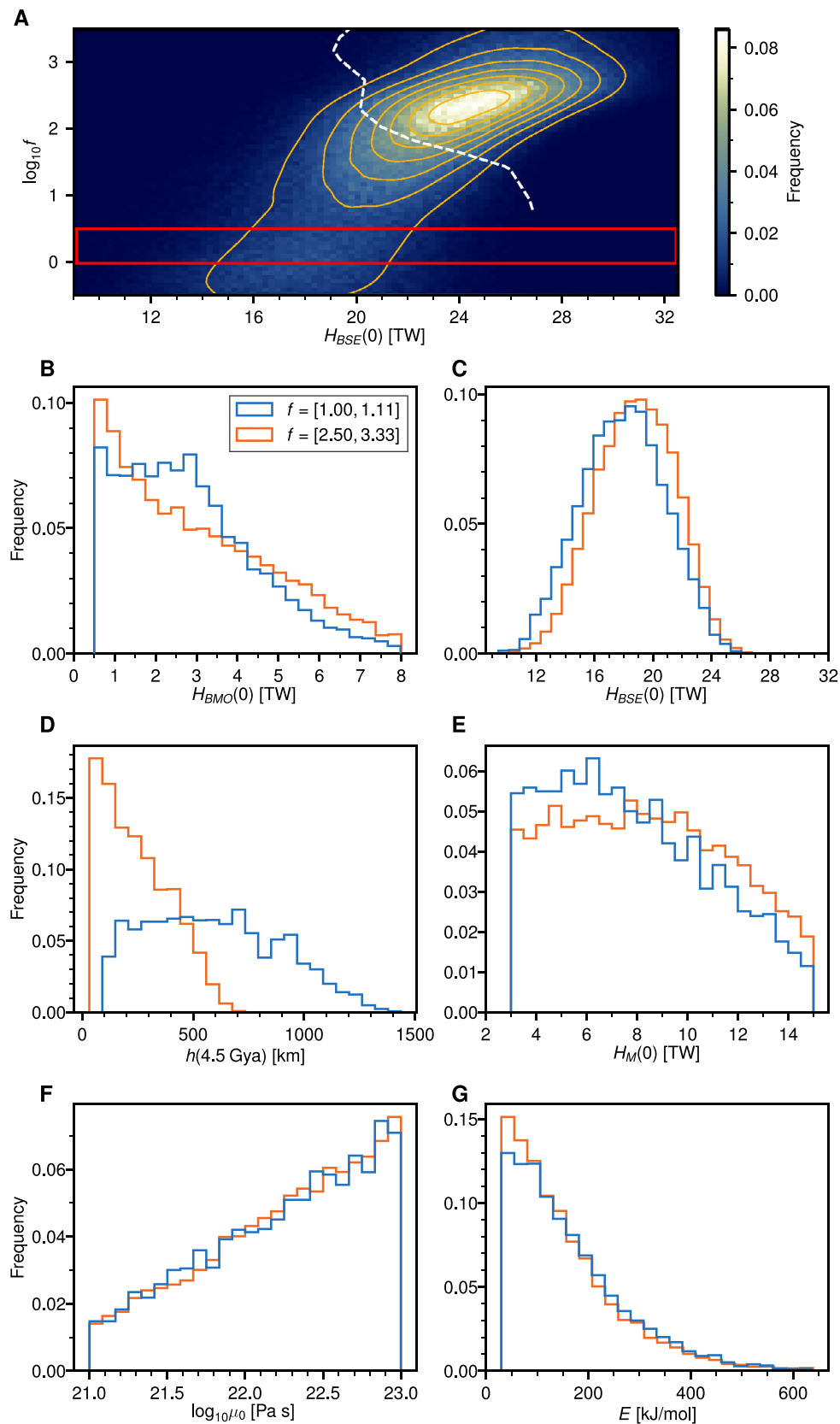


**Fig. 3.** Parameter distributions of successful models. (a) Enrichment parameter  $f$  as a function of BSE heat production for all models satisfying the mantle temperature constraint. Beige contour lines denote every 0.01 on the frequency scale. The red box contains the two successful ranges of  $f$ . The dashed white contour line divides cases where core heat flux is positive at 2.5 Gya (left of contour) and cases where core heat flux is negative at 2.5 Gya (right of contour). (b–g) Parameter distributions for models that satisfy both the mantle temperature constraint and the  $H_{BSE}$  self-consistency constraint. (b) Melt layer heat production, (c) BSE heat production, (d) initial melt layer thickness, (e) solid mantle heat production, (f) reference lower mantle viscosity, and (g) effective activation enthalpy. Here, the case with constant mantle heat flux through Earth history is shown; the two heat flux cases yield effectively the same parameter distributions. Additional parameters are plotted in Fig. S4.

**Table 3**  
Parameter means and standard deviations of successful runs for the case of constant surface heat flux.

Parameter	Unit	$f = [1.00, 1.11]$		$f = [2.50, 3.33]$	
		Mean	$1\sigma$	Mean	$1\sigma$
$H_{BMO}(0)$	TW	2.81	1.60	3.00	1.88
$H_{CC}(0)$	TW	7.32	1.40	7.41	1.44
$H_M(0)$	TW	7.80	3.08	8.40	3.20
$H_{BSE}(0)$	TW	17.93	2.84	18.81	2.69
$Q_{tot}(0)$	TW	46.20	1.71	46.11	1.71
$H_{BMO0}/M_{BMO}(0)$	$10^{-12}$ W/kg	459	283	490	329
$H_M(0)/M_M(0)$	$10^{-12}$ W/kg	1.9	0.8	2.1	0.8
$dT/dz$	K/km	$3.55 \times 10^{-4}$	$0.29 \times 10^{-4}$	$3.54 \times 10^{-4}$	$0.28 \times 10^{-4}$
$E$	kJ/mol	163	109	154	107
$V$	$m^3/mol$	$3.21 \times 10^{-6}$	$2.38 \times 10^{-6}$	$2.67 \times 10^{-6}$	$2.17 \times 10^{-6}$
$\log_{10} \mu_0$	Pa s	22.23	0.54	22.25	0.53
$h(0)$	km	7.60	1.43	7.61	1.44
$T_L(0)$	K	3511	267	3556	276
$T_A$	K	5460	288	5470	289
$T_B$	K	3542	288	3531	287
$\Delta\xi$		0.110	0.074	0.123	0.08
$\kappa_g$	1/Gyr	8.83	4.73	8.76	4.76
$C_C$	J/kg/K	722	100	727	101
$F_{IC}$	J/kg	$1.25 \times 10^6$	$0.43 \times 10^6$	$1.25 \times 10^6$	$0.43 \times 10^6$
$f$	TW	1.055	0.032	2.894	0.241
$h(4.5 \text{ Gya})$	km	592	294	247	151

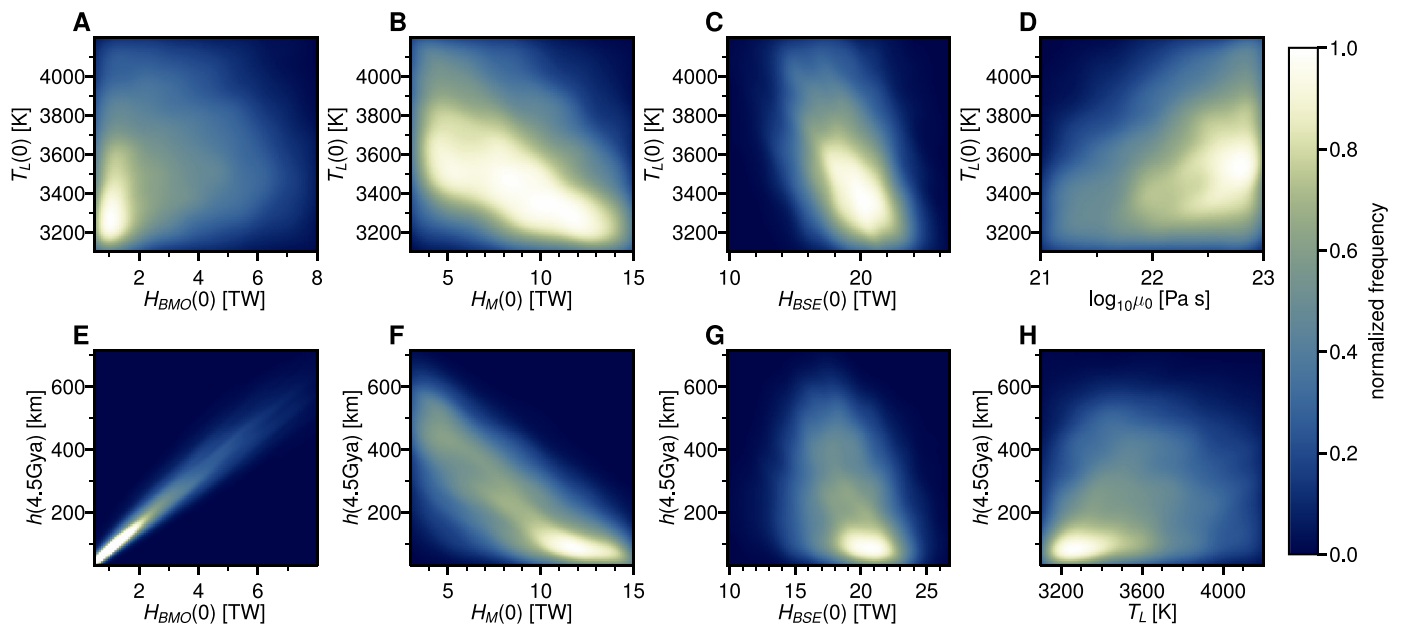


**Fig. 4.** Selected parameter correlations for the case where  $2.5 < f < 3.33$  and surface heat flux is constant through Earth history. The remaining  $f$  and heat flux cases exhibit similar parameter correlations. Color indicates frequency among successful cases; each panel is normalized to a maximum frequency of 1.

of  $20 \pm 4$  TW, but this estimate is not based on a valid statistical analysis (see section 3.1 of Lyubetskaya and Korenaga (2007)). In the present study, a Monte Carlo approach, paired with mantle temperature constraints and a physical bound on the degree of fractional crystallization, has allowed for geodynamical estimates of  $H_{BSE}$  in the presence of a BMO:  $19 \pm 3$  TW or  $18 \pm 3$  TW, depending on the mechanism of BMO formation. Though the new estimate overlaps with the traditional estimates, a logically consistent estimate even with a hidden geochemical reservoir allows us to probe more deeply the thermal and chemical evolution of Earth's mantle. For example, in addition to present-day  $H_{BSE}$ , we are able to constrain present-day  $H_M$ , which represents the combination of heat production in DMM and EM. When combined with estimates of heat-producing element concentrations in DMM and EM, the value of  $H_M$  can be used to constrain the relative proportion of these two reservoirs within the mantle.  $H_M$  depends on BMO formation mechanism; for the case of  $f = [1, 1.11]$ ,  $H_M$  is

commonly as low as 3 TW, whereas for the case of  $f = [2.5, 3.33]$ ,  $H_M$  is typically in the range 6–10 TW (Fig. 3E). If  $H_M$  is 3 TW, then the entire heat budget of the mantle can be explained by DMM, assuming reasonable concentrations of heat-producing elements in DMM (Salters and Stracke, 2004; Workman and Hart, 2005); the proportion of EM vanishes. On the other hand, if  $H_M \geq 6$  TW, then EM may make up a substantial portion of the mantle, depending on its composition. Such constraints on mantle composition bear importance for global-scale mantle dynamics and geochemistry.

The above uncertainty of heat production in the convecting mantle propagates directly to all other refractory lithophile elements and indirectly to the rest of the elements, because the BSE concentrations of most elements are derived from the concentrations of refractory lithophile elements. Thus, the BMO hypothesis necessitates a revision of BSE composition models. Such a revision, however, requires melt-solid partition coefficients at lower mantle

conditions, because most elements are not as highly incompatible as heat-producing elements, and experimental constraints are both scarce and highly uncertain (e.g., Andraut et al. (2012); Tateno et al. (2014)).

Revising BSE composition models will also require  $H_{BSE}$  constraints with a higher degree of certainty than the present study establishes. For example, uncertainties afflicting our model include the mechanism of BMO formation, observational or experimental estimates of various lower mantle and core parameters, and vigor of Hadean plate tectonics. The mechanism driving BMO formation is still highly uncertain, as it must be assessed theoretically and requires knowledge of grain sizes and viscosity in a crystallizing magma ocean as well as crystal-melt partitioning at high pressures (Miyazaki and Korenaga, 2019). While BMO formation scenario, represented by the two ranges of  $f$  that we consider, does not significantly influence most aspects of thermal evolution, it does appear to control initial BMO thickness (Fig. 3D) and the budget of heat-producing elements in the solid mantle (Fig. 3E), the importance of which has been discussed above. Lower mantle viscosity is also largely uncertain due to experimental limitations. We consider lower mantle viscosities spanning two orders of magnitude, and this entire range appears in the ensemble of successful models (Fig. 3F). Lower mantle viscosity correlates with melt layer temperature (Fig. 4D), so improvements on lower mantle viscosity estimates may help constrain thermal evolution. Core heat capacity and energy from core formation also suffer from uncertainty, although these parameters do not significantly influence model results (correlations between these parameters and others are low; see Tables S2 and S3). Finally, the history of surface heat flux is unclear. While several observational lines of evidence point to constant surface heat flux through most of Earth's history (see Methods), higher surface heat flux in the Hadean cannot be ruled out. Luckily, successful models are insensitive to which surface heat flux history is applied (see Results).

It is important to note the role that key assumptions play in our model. For one, we do not consider thermochemical piles (i.e., LLSVPs), which would influence the parameterization of core-mantle boundary heat flux. Specifically, thermochemical piles act as thermal insulators, so that CMB heat flux is dominated by regions not occupied by piles (e.g., Li et al., 2018). Thus, incorporating piles into our model would reduce heat flux into the solid mantle (assuming the temperature structure remains unchanged in lower mantle regions not occupied by piles). A given model would therefore yield a more long-lived inner core as a result of this reduced CMB heat flux. Another key assumption we make is that a crystallizing BMO is the only hidden geochemical reservoir; it is possible that there are additional unsampled mantle reservoirs, as previously noted (e.g., LLSVPs and/or BEAMS, if they do not originate from a BMO). Thus, further study into the origin and evolution of these lower mantle features, and thus their potential as hidden geochemical reservoirs, are warranted. For example, the chemical density anomaly of LLSVPs, and their role in geodynamical processes, are poorly known. Nonetheless, the present study offers a novel approach that can be combined with future advancements in these areas to further constrain  $H_{BSE}$  in the presence of a hidden geochemical reservoir.

In pursuit of evaluating the validity of  $H_{BSE}$  estimates that assume a BMO, an important task is to obtain an observational backing for BMO-originated ULVZs. An observational underpinning is especially crucial given the controversial nature of ULVZs. For example, it is unclear whether the dynamics of a partial melt layer suggest physical properties consistent with observations of ULVZs (Hernlund and Tackley, 2007; Hernlund and Jellinek, 2010), and thus whether the BMO hypothesis is dynamically feasible. Geoneutrino detection could provide a critical test; geoneutrinos are emitted by radioactive decay and thus reflect the abundances of heat-

producing elements in Earth (Gando et al., 2011). We predict that ULVZs are highly concentrated in heat-producing elements—over 100 times more concentrated than the solid mantle (Table 3). This is a natural consequence of melt crystallization, which leads to enrichment in incompatible elements of the melt over time. Therefore, with continuing improvement in detection capabilities (e.g., Šrámek et al., 2016; Abe et al., 2022), geoneutrino measurements offer a promising approach to testing the BMO hypothesis for ULVZs.

## Funding

U.S. National Science Foundation grant EAR-1753916 (JK).

## CRediT authorship contribution statement

**Amy L. Ferrick:** Investigation, Methodology, Visualization, Writing – original draft, Writing – review & editing. **Jun Korenaga:** Methodology, Supervision, Writing – review & editing.

## Declaration of competing interest

The authors declare that they have no known competing financial interests or personal relationships that could have appeared to influence the work reported in this paper.

## Data and materials availability

All data are available in the main text or the supplementary materials.

## Appendix A. Supplementary material

Supplementary material related to this article can be found online at <https://doi.org/10.1016/j.epsl.2022.117893>.

## References

- Abe, S., Asami, S., Eizuka, M., Futagi, S., Gando, A., et al., 2022. Abundances of uranium and thorium elements in Earth estimated by geoneutrino spectroscopy. *Geophys. Res. Lett.* 49, e2022GL099566.
- Albarède, F., van der Hilst, R.D., 2002. Zoned mantle convection. *Philos. Trans. R. Soc. Lond. A* 360, 2569–2592.
- Allègre, C.J., Hofmann, A., O'Nions, K., 1996. The argon constraints on mantle structure. *Geophys. Res. Lett.* 23 (24), 3555–3557.
- Andraut, D., Petitgirard, S., Nigro, G.L., Devidal, J.-L., Veronesi, G., Garbarino, G., Mezouar, M., 2012. Solid-liquid iron partitioning in Earth's deep mantle. *Nature* 487, 354–357.
- Ballmer, M.D., Lourenço, D.L., Hirose, K., Caracas, R., Nomura, R., 2017. Reconciling magma-ocean crystallization models with the present-day structure of the Earth's mantle. *Geochem. Geophys. Geosyst.* 18, 2785–2806.
- Boyett, M., Carlson, R.W., 2005.  $^{142}\text{Nd}$  evidence for early (>4.53 Ga) global differentiation of the silicate Earth. *Science* 309, 576–581.
- Bradley, D.C., 2008. Passive margins through Earth history. *Earth-Sci. Rev.* 91, 1–26.
- Buffett, B.A., Garnero, E.J., Jeanloz, R., 2000. Sediments at the top of Earth's core. *Science* 290, 1338–1342.
- Condie, K., Pisarevsky, S.A., Korenaga, J., Gardoll, S., 2015. Is the rate of supercontinent assembly changing with time? *Precambrian Res.* 259, 278–289.
- Dobson, D.P., Brodholt, J.P., 2005. Subducted banded iron formations as a source of ultralow-velocity zones at the core-mantle boundary. *Nature* 434, 371–374.
- Dobson, D.P., Dohman, R., Wiedenbeck, M., 2008. Self-diffusion of oxygen and silicon in  $\text{MgSiO}_3$  perovskite. *Earth Planet. Sci. Lett.* 270 (1–2), 125–129.
- Driscoll, P., Bercowski, D., 2014. On the thermal and magnetic histories of Earth and Venus: influences of melting, radioactivity, and conductivity. *Phys. Earth Planet. Inter.* 236, 36–51.
- Dziewonski, A.M., Anderson, D.L., 1981. Preliminary reference Earth model. *Phys. Earth Planet. Inter.* 25, 297–356.
- Fiquet, G., Auzende, A.L., Siebert, J., Corgne, A., Bureau, H., Ozawa, H., Garbarino, G., 2010. Melting of peridotite to 140 gigapascals. *Science* 329, 1516–1518.
- Forte, A.M., Simmons, N.A., Grand, S.P., 2015. Constraints on 3-D seismic models from global geodynamic observables: Implications for the global mantle convective flow. In: Romanowicz, B., Dziewonski, A. (Eds.), *Treatise on Geophysics*, vol. 1, second edition. Elsevier, Amsterdam, pp. 853–907.

- Gando, A., Dwyer, D., McKeown, R., Zhang, C., 2011. Partial radiogenic heat model for Earth revealed by geoneutrino measurements. *Nat. Geosci.* 4, 647–651.
- Garnero, E.J., Revenaugh, J., Williams, Q., Lay, T., Kellogg, L.H., 1998. Ultralow velocity zone at the core-mantle boundary. In: Gurnis, M., Wysession, M.E., Knittle, E., Buffet, B.A. (Eds.), *The Core-Mantle Boundary Region*. American Geophysical Union, pp. 319–334.
- Gülcher, A.J.P., Ballmer, M.D., Tackley, P.J., 2021. Coupled dynamics and evolution of primordial and recycled heterogeneity in Earth's lower mantle. *Solid Earth* 12, 2087–2107.
- Hernlund, J.W., Tackley, P.J., 2007. Some dynamical consequences of partial melting in Earth's deep mantle. *Phys. Earth Planet. Inter.* 162, 149–163.
- Hernlund, J.W., Jellinek, A.M., 2010. Dynamics and structure of a stirred partially Molten ultralow-velocity zone. *Earth Planet. Sci. Lett.* 296, 1–8.
- Herzberg, C., Condie, K., Korenaga, J., 2010. Thermal history of the Earth and its petrological expression. *Earth Planet. Sci. Lett.* 292, 79–88.
- Kaminski, E., Javoy, M., 2013. A two-stage scenario for the formation of the Earth's mantle and core. *Earth Planet. Sci. Lett.* 365, 97–107.
- Karato, S.-I., 2008. *Deformation of Earth Materials: An Introduction to the Rheology of Solid Earth*. Cambridge University Press.
- Karki, B.B., Khanduja, G., 2007. A computational study of ionic vacancies and diffusion in MgSiO<sub>3</sub> perovskite and post-perovskite. *Earth Planet. Sci. Lett.* 260 (1–2), 201–211.
- Korenaga, J., 2005. Firm mantle plumes and the nature of the core–mantle boundary region. *Earth Planet. Sci. Lett.* 232, 29–37.
- Korenaga, J., 2008. Urey ratio and the structure and evolution of Earth's mantle. *Rev. Geophys.* 46, RG2007.
- Korenaga, J., 2009. A method to estimate the composition of the bulk silicate Earth in the presence of a hidden geochemical reservoir. *Geochim. Cosmochim. Acta* 73, 6952–6964.
- Korenaga, J., 2021. Hadean geodynamics and the nature of early continental crust. *Precambrian Res.* 359, 106178.
- Labrosse, S., 2003. Thermal and magnetic evolution of Earth's core. *Phys. Earth Planet. Inter.* 140, 127–143.
- Labrosse, S., Hernlund, J., Coltice, N., 2007. A crystallizing dense magma ocean at the base of the Earth's mantle. *Nature* 450, 866–869.
- Labrosse, S., Hernlund, J.W., Hirose, K., 2015. Fractional melting and freezing in the deep mantle and implications for the formation of a basal magma ocean. In: Badro, J., Walter, M. (Eds.), *The Early Earth: Accretion and Differentiation*, vol. 212. American Geophysical Union, pp. 123–142.
- Labrosse, S., Morison, A., Deguen, R., Alboussière, T., 2018. Rayleigh–Bénard convection in a creeping solid with melting and freezing at either or both its horizontal boundaries. *J. Fluid Mech.* 846, 5–36.
- Lay, T., Garnero, E.J., Williams, Q., 2004. Partial melting in a thermo-chemical boundary layer at the base of the mantle. *Phys. Earth Planet. Inter.* 146, 441–467.
- Li, M., Zhong, S., Olson, P., 2018. Linking lowermost mantle structure, core-mantle boundary heat flux and mantle plume formation. *Phys. Earth Planet. Inter.* 277, 10–29.
- Liu, J., Li, J., Hrubciak, R., Smith, J.S., 2016. Origins of ultralow velocity zones through slab-derived metallic melt. *Proc. Natl. Acad. Sci. USA* 113, 5547–5551.
- Lyubetskaya, T., Korenaga, J., 2007. Chemical composition of Earth's primitive mantle and its variance: 1. Method and results. *J. Geophys. Res.* 112, B03211.
- Mao, W.L., Mao, H.-K., Sturhahn, W., Zhao, J., Prakapenka, V.B., Meng, Y., Shu, J., Fei, Y., Hemley, R.J., 2006. Iron-rich post-perovskite and the origin of ultralow-velocity zones. *Science* 312, 564–565.
- Mashino, I., Murakami, M., Miyajima, N., Petitgirard, S., 2020. Experimental evidence for silica-enriched Earth's lower mantle with ferrous iron dominant bridgmanite. *Proc. Natl. Acad. Sci. USA* 117, 27899–27905.
- McDonough, W.F., Sun, S.-S., 1995. The composition of the Earth. *Chem. Geol.* 120, 223–253.
- Miyazaki, Y., Korenaga, J., 2019. On the timescale of magma ocean solidification and its chemical consequences: 2. Compositional differentiation under crystal accumulation and matrix compaction. *J. Geophys. Res., Solid Earth* 124, 3399–3419.
- Miyazaki, Y., Korenaga, J., 2022. A wet heterogeneous mantle creates a habitable world in the Hadean. *Nature* 603, 86–90.
- Mosenfelder, J.L., Asimow, P.D., Frost, D.J., Rubie, D.C., Ahrens, T.J., 2009. The Mg-SiO<sub>3</sub> system at high pressure: thermodynamic properties of perovskite, postperovskite, and melt from global inversion of shock and static compression data. *J. Geophys. Res.* 114, B01203.
- Murakami, M., Ohishi, Y., Hirao, N., Hirose, K., 2012. A perovskitic lower mantle inferred from high-pressure, high-temperature sound velocity data. *Nature* 485, 90–94.
- O'Nions, R.K., Oxburgh, E.R., 1983. Heat and helium in the Earth. *Nature* 306, 429–431.
- Otsuka, K., Karato, S.-I., 2012. Deep penetration of Molten iron into the mantle caused by a morphological instability. *Nature* 492, 243–246.
- Pachhai, S., Li, M., Thorne, M.S., Dettmer, J., Tkaličić, H., 2021. Internal structure of ultra-low velocity zones consistent with origin from a basal magma ocean. *Nat. Geosci.* 15, 79–84.
- Padhi, C.M., Korenaga, J., Ozima, M., 2012. Thermal evolution of Earth with xenon degassing: a self-consistent approach. *Earth Planet. Sci. Lett.* 341–344, 1–9.
- Palme, H., O'Neill, H.S.C., 2003. Cosmochemical estimates of mantle composition. In: Carlson, R.W. (Ed.), *Treatise on Geochemistry*, vol. 2. Elsevier, Amsterdam, pp. 1–38.
- Pehrsson, S.J., Eglinton, B.M., Evans, D.A., Huston, D., Reddy, S.M., 2016. Metallogeny and its link to orogenic style during the Nuna supercontinent cycle. *Geol. Soc. (Lond.) Spec. Publ.* 424, 83–94.
- Rosas, J.C., Korenaga, J., 2018. Rapid crustal growth and efficient crustal recycling in the early Earth: implications for Hadean and Archean geodynamics. *Earth Planet. Sci. Lett.* 494, 42–49.
- Salters, V.J.M., Stracke, A., 2004. Composition of the depleted mantle. *Geochem. Geophys. Geosyst.* 5 (5), Q05B07.
- Sleep, N.H., Zahnle, K., Neuhoff, P., 2001. Initiation of clement surface conditions on the earliest Earth. *Proc. Natl. Acad. Sci.* 98, 3666–3672.
- Solomatov, V., 1996. Can hotter mantle have a larger viscosity? *Geophys. Res. Lett.* 23, 937–940.
- Solomatov, V., 2015. Magma oceans and primordial mantle differentiation. In: Solomatov, V. (Ed.), *Treatise on Geophysics*, vol. 9, 2nd ed. Elsevier, Amsterdam, pp. 91–119.
- Šrámek, O., Roskovec, B., Wipperfurth, S.A., Xi, Y., McDonough, W.F., 2016. Revealing the Earth's mantle from the tallest mountains using the Jinping Neutrino Experiment. *Sci. Rep.* 6, 33034.
- Stevenson, D.J., Spohn, T., Schubert, G., 1983. Magnetism and thermal evolution of the terrestrial planets. *Icarus* 54, 466–489.
- Tarduno, J., Cottrell, R., Watkeys, M., Bauch, D., 2007. Geomagnetic field strength 3.2 billion years ago recorded by single silicate crystals. *Nature* 446, 657–660.
- Tateno, S., Hirose, K., Ohishi, Y., 2014. Melting experiments on peridotite to lowermost mantle conditions. *J. Geophys. Res., Solid Earth* 119, 4684–4694.
- Thorne, M.S., Garnero, E.J., 2004. Inferences on ultralow-velocity zone structure from a global analysis of SPdKS waves. *J. Geophys. Res.* 109, B08301.
- Wicks, J.K., Jackson, J.M., Sturhahn, W., Zhang, D., 2017. Sound velocity and density of magnesiowüstites: implications for ultralow-velocity zone topography. *Geophys. Res. Lett.* 44, 2148–2158.
- Williams, Q., Garnero, E.J., 1996. Seismic evidence for partial melt at the base of Earth's mantle. *Science* 273, 1528–1530.
- Workman, R.K., Hart, S.R., 2005. Major and trace element composition of the depleted MORB mantle (DMM). *Earth Planet. Sci. Lett.* 231, 53–72.